







Article

Electrochemical Investigations of $\text{BaCe}_{0.7-x}\text{Sm}_x\text{Zr}_{0.2}\text{Y}_{0.1}\text{O}_{3-\delta}$ Sintered at a Low Sintering Temperature as a Perovskite Electrolyte for IT-SOFCs

Muneeb Irshad ¹, Mehak Khalid ¹, Muhammad Rafique ², Asif Nadeem Tabish ³ , Ahmad Shakeel ^{3,4,*} , Khurram Siraj ¹ , Abdul Ghaffar ⁵, Rizwan Raza ⁶ , Muhammad Ahsan ⁷, Quar tul Ain ¹  and Qurat ul Ain ¹ 

- ¹ Department of Physics, University of Engineering and Technology, Lahore 54890, Pakistan; muneebirshad@gmail.com (M.I.); mhhkhalid130@gmail.com (M.K.); khurram.uet@gmail.com (K.S.); quartulain98@gmail.com (Q.t.A.); quratulainquratulain786@gmail.com (Q.u.A.)
 - ² Department of Physics, University of Sahiwal, Sahiwal 57000, Pakistan; mrafique.uet@gmail.com
 - ³ Department of Chemical Engineering, New Campus, University of Engineering and Technology, Lahore 39021, Pakistan; antabish@uet.edu.pk
 - ⁴ Faculty of Civil Engineering and Geosciences, Department of Hydraulic Engineering, Delft University of Technology, Stevinweg 1, 2628 CN Delft, The Netherlands
 - ⁵ Department of Physics, Government College University, Lahore 54000, Pakistan; abdulghaffar@gcu.edu.pk
 - ⁶ Clean Energy Research Lab (CERL), Department of Physics, Lahore Campus, COMSATS University Islamabad, Lahore 54000, Pakistan; razahussaini786@gmail.com
 - ⁷ Department of Thermal Power and Energy Engineering, Huazhong University of Science and Technology, Wuhan 430074, China; ahsan@hust.edu.cn
- * Correspondence: a.shakeel@tudelft.nl



Citation: Irshad, M.; Khalid, M.; Rafique, M.; Tabish, A.N.; Shakeel, A.; Siraj, K.; Ghaffar, A.; Raza, R.; Ahsan, M.; Ain, Q.t.; et al. Electrochemical Investigations of $\text{BaCe}_{0.7-x}\text{Sm}_x\text{Zr}_{0.2}\text{Y}_{0.1}\text{O}_{3-\delta}$ Sintered at a Low Sintering Temperature as a Perovskite Electrolyte for IT-SOFCs. *Sustainability* **2021**, *13*, 12595. <https://doi.org/10.3390/su132212595>

Academic Editor: Changhyun Roh

Received: 4 October 2021

Accepted: 10 November 2021

Published: 15 November 2021

Publisher's Note: MDPI stays neutral with regard to jurisdictional claims in published maps and institutional affiliations.



Copyright: © 2021 by the authors. Licensee MDPI, Basel, Switzerland. This article is an open access article distributed under the terms and conditions of the Creative Commons Attribution (CC BY) license (<https://creativecommons.org/licenses/by/4.0/>).

Abstract: Perovskite materials have gained a lot of interest in solid oxide fuel cell (SOFC) applications owing to their exceptional properties; however, ideal perovskites exhibit proton conduction due to availability of low oxygen vacancies, which limit their application as SOFC electrolytes. In the current project, Sm was doped at the B-site of a $\text{BaCe}_{0.7-x}\text{Sm}_x\text{Zr}_{0.2}\text{Y}_{0.1}\text{O}_{3-\delta}$ perovskite electrolyte for intermediate-temperature solid oxide fuel cells (IT-SOFCs). $\text{BaCe}_{0.7-x}\text{Sm}_x\text{Zr}_{0.2}\text{Y}_{0.1}\text{O}_{3-\delta}$ electrolytes were synthesized through a cost-effective coprecipitation method and were sintered at a low sintering temperature. The effects of samarium (Sm) doping on the electrochemical performance of $\text{BaCe}_{0.7-x}\text{Sm}_x\text{Zr}_{0.2}\text{Y}_{0.1}\text{O}_{3-\delta}$ were investigated. X-ray diffraction (XRD) analysis confirmed that the $\text{BaCe}_{0.7-x}\text{Sm}_x\text{Zr}_{0.2}\text{Y}_{0.1}\text{O}_{3-\delta}$ electrolyte material retained the perovskite structure. The secondary phase of Sm_2O_3 was observed for $\text{BaCe}_{0.4}\text{Sm}_{0.3}\text{Zr}_{0.2}\text{Y}_{0.1}\text{O}_{3-\delta}$. Scanning electron microscopic (SEM) imaging displayed the dense microstructure for all the compositions, while prominent crystal growth was observed for composition $x = 0.3$. The formation of the perovskite structure and the presence of the hydroxyl groups of metal oxides for all the compositions were confirmed by Fourier transform infrared spectroscopy (FTIR). An increased symmetrical disturbance was also observed for the increased doping ratio of the Sm. Thermogravimetric analysis (TGA) of all the compositions showed no major weight loss in the SOFC operating temperature range. It was also noted that the conductivity of $\text{BaCe}_{0.7-x}\text{Sm}_x\text{Zr}_{0.2}\text{Y}_{0.1}\text{O}_{3-\delta}$ gradually decreased with the increased contents of the Sm metal. The maximum power density of 390 mW cm^{-2} , and an open-circuit voltage (OCV) of 1.0 V at 600°C , were obtained, showing that $\text{BaCe}_{0.7-x}\text{Sm}_x\text{Zr}_{0.2}\text{Y}_{0.1}\text{O}_{3-\delta}$, synthesized by a cost-effective method and sintered at a low temperature, can be used as a proton-conducting electrolyte for IT-SOFCs.

Keywords: perovskite; electrolyte; coprecipitation; composite; SOFC

1. Introduction

During the last decade, the energy demand increased exponentially because of worldwide economic developments and rapid industrial growth. The developed countries are fulfilling their energy needs through nonrenewable sources, such as fossil fuels, coal,

gas, etc. However, natural resources are depleting rapidly. The increased utilization of conventional energy sources is also causing global warming because of the emission of harmful gases, such as CO_2 , into the atmosphere [1–3]. Therefore, the most critical and urgent concern for engineers and scientists is to find renewable energy sources that can overcome these problems. Renewable energy sources are preferred because of their low cost and environment-friendly aspects. Fuel cells are preferred among different energy sources because of their high efficiency, durability, fuel flexibility, and eco-friendly nature. Moreover, they are considered advantageous because of their reliability, longer lifetime, cost-effectiveness, low noise, and zero air pollution [4–7]. In SOFCs, the electrolytes have a vital role in the cell performance because of their high ionic and protonic conductivity. Many materials cannot fulfill the requirements that are necessary for SOFCs electrolyte, at high operating temperatures, but they can be used for low operating temperatures through modifications [8–11].

The proton-conducting electrolyte has gained a lot of importance because of its low activation energy and high conductivity. Perovskite structure materials are mostly proton-conducting electrolytes. The chemical formula for perovskite is ABO_3 , where A and B are the cations of metal-oxide, with charges of +2 or +3, and +4 or +3, respectively. The size of the O-site anion is analogous to the A-cation. Barium-based perovskite materials are preferred because of their high ionic conductivity and oxygen storage capacity compared to barium zirconate. The protonic conductivity of these materials, when doped with different rare earth elements and transition metals, can be enhanced [12,13].

The perfect ABO_3 perovskites (A = Ca, Ba, Sr; B = Ce, Zr) have low oxygen vacancies and, therefore, have low proton conduction. The B site doping can increase the oxygen vacancies within lattices because of the charge compensation associated with higher structural distortion. The Goldschmidt tolerance factor (t) is a far and wide accepted criterion for the perovskite structure, and an ideal cubic perovskite structure exhibits $t = 1$. However, many perovskite materials deviate from the ideal structure and exhibit disordered structures upon doping [14]. The dopant concentration also changes the microstructure, ionic conductivity, and thermal stability of electrolytes. The ionic conductivity of perovskite materials also depends on the charge carrier concentration, activation energy, the trapping effect between the host and dopant, lattice expansion or lattice distortion, grain size and grain boundary, etc. [15–17]. Researchers have reported that a yttrium-doped barium cerium zirconate (BCZY) proton-conducting electrolyte showed high stability and good proton conductivity, among other materials. When rare earth elements are doped with a trivalent cation, such as samarium, yttrium, gadolinium, neodymium, etc., it produces enough oxygen ion vacancies in the perovskites structure, which increases the proton conductivity [18–20].

Samarium, as a dopant in barium-cerate-type materials, is used to improve the ionic conductivity and becomes highly proton-conductive under the influence of a hydrogen atmosphere [21]. It has also been reported that an appropriate dopant level of samarium is necessary because the high doping ratio of Sm increases the lattice distortion [22]. Mostly, the lanthanide materials in the perovskite structure partition over the A and B sites, which decreases the oxygen vacancies and, therefore, ionic conductivity decreases [23]. It is also reported that doping in a barium cerate proton-conducting electrolyte leads to larger grain sizes and reduces the contribution of ions to the facial area [24].

K. Lee et. al. fabricated SOFC cells having a spin-coated $\text{BaCe}_{0.6}\text{Zr}_{0.2}\text{Y}_{0.2}\text{O}_{3-\delta}$ proton-conducting electrolyte, using NiO as a sintering aid. The fabricated SOFC exhibited a maximum power density of 106.6 mWcm^{-2} at 800°C , using humidified H_2 (3% H_2O) [25]. Zhijun et. al. investigated the effects of Ni and Fe additives on $\text{BaCe}_0\text{Zr}_{0.1}\text{Y}_{0.2}\text{O}_{3-\delta}$ and attained a power density of 120 mWcm^{-2} at 450°C using humidified H_2 (3% H_2O) [26]. The researchers reported a power density of 410 mWcm^{-2} for a $\text{BaCe}_{0.7}\text{XZr}_{0.1}\text{Y}_{0.2-x}\text{O}_3$ proton-conducting electrolyte synthesized by the solid-state reactive method, with humidified H_2 (5% H_2O) at 600°C [22]. Amir et.al. fabricated a tubular fuel cell using

a $\text{BaZr}_{0.1}\text{Ce}_{0.7}\text{Y}_{0.1}\text{Yb}_{0.1}\text{O}_3$ electrolyte (25 μm thickness) and attained a power density of 331 mWcm^{-2} at $600\text{ }^\circ\text{C}$ using humidified H_2 (3% H_2O) [27].

This work is also an effort to investigate $\text{BaCe}_{0.7-x}\text{Sm}_x\text{Zr}_{0.2}\text{Y}_{0.1}\text{O}_{3-\delta}$ as a stoichiometric material with the doping of Sm through the coprecipitation method. The objective of this project was to increase the conductivity of $\text{BaCe}_{0.7-x}\text{Sm}_x\text{Zr}_{0.2}\text{Y}_{0.1}\text{O}_{3-\delta}$ by increasing the oxygen vacancies with Sm doping, while retaining the perovskite structure using a cost- and time-effective synthesis route. The coprecipitation method was adapted to synthesize the fine $\text{BaCe}_{0.7-x}\text{Sm}_x\text{Zr}_{0.2}\text{Y}_{0.1}\text{O}_{3-\delta}$ powder materials, which were then sintered at a lower temperature than the reported temperatures. The synthesized $\text{BaCe}_{0.7-x}\text{Sm}_x\text{Zr}_{0.2}\text{Y}_{0.1}\text{O}_{3-\delta}$ retained its perovskite structure upon Sm doping, and increased conductivity was obtained. Under the possible parameters of the synthesis and measurements, the role of Sm as a dopant on the properties of $\text{BaCe}_{0.7-x}\text{Sm}_x\text{Zr}_{0.2}\text{Y}_{0.1}\text{O}_{3-\delta}$ is reported here.

2. Experimental

The proton-conducting electrolyte material of $\text{BaCe}_{0.7-x}\text{Sm}_x\text{Zr}_{0.2}\text{Y}_{0.1}\text{O}_{3-\delta}$ ($x = 0, 0.1, 0.2, 0.3$) was synthesized by the coprecipitation method. The starting materials used for synthesis were Ba (NO_3)₂ (Unichem, Mumbai, India, >99%), Ce (NO_3)₃·6H₂O (Alfa Aesar, Haverhill, MA, USA, >99%), Zr (NO_3)₂·6H₂O (Sigma-Aldrich, St. Louis, MO, USA, >99%), Y (NO_3)₃·6H₂O (Alfa Aesar, >99%), and Sm (NO_3)₃·6H₂O (Alfa Aesar, >99%). The stoichiometric amount of precursor materials was added to the deionized water under constant heating and stirring at $90\text{ }^\circ\text{C}$. The mixture was stirred until a transparent solution was formed. Sodium carbonate was added separately in deionized water as a precipitation agent, and the solution was then added, drop by drop, with continuous stirring, leading to the formation of precipitates. The prepared precipitates were then extracted by Whatman filter paper (Grade 1) and washed with deionized water twice. The obtained $\text{BaCe}_{0.7-x}\text{Sm}_x\text{Zr}_{0.2}\text{Y}_{0.1}\text{O}_{3-\delta}$ powder was then calcined for 1 h at $150\text{ }^\circ\text{C}$ to get the dehydrated powder, and later sintered for 4 h at $1200\text{ }^\circ\text{C}$. Fine $\text{BaCe}_{0.7-x}\text{Sm}_x\text{Zr}_{0.2}\text{Y}_{0.1}\text{O}_{3-\delta}$ powder were obtained after crushing sintered electrolyte materials in a mortar pestle. Pellets were obtained by the uniaxial pressing of the hydraulic press at a pressure of about 300 MPa. Figure 1 represents the flowchart of the synthesis process.

Different characterization techniques were employed to examine the properties of the obtained samples. SEM micrographs were by SEM (Hitachi 3000 H, Hitachi, Chiyoda City, Japan) to analyze the microstructure and surface morphology. The crystal structure and crystallite size were determined through a XRD diffractometer (PANalytical Malvern Panalytical, Malvern, UK). A thermogravimetric analysis (TGA Q500, TA Instruments, New Castle, DE, USA) was employed to investigate the weight loss in the temperature range of $30\text{--}900\text{ }^\circ\text{C}$. Fourier transform infrared spectroscopy (JASCO 4600, Tokyo, Japan) was employed to find the functional groups of the metal oxides and the stability of the perovskite structure. The ionic conductivity of all prepared samples was determined through four-probe DC method.

Cell Fabrication and Testing

The performance was evaluated at $600\text{ }^\circ\text{C}$ by fabricating button cells having electrolyte material, $\text{BaCe}_{0.7-x}\text{Sm}_x\text{Zr}_{0.2}\text{Y}_{0.1}\text{O}_{3-\delta}$ ($x = 0\text{--}0.3$), using uniaxial pressing. The materials used as anode and cathode were Ni-BCZY and LSC, respectively. The thickness of each button cell was 1.5 mm, with a diameter of 13 mm. Nickel foil was used alongside the anode to avoid cell breakage. Humidified hydrogen (~3% H_2O) was provided as a fuel, with a flow rate of 50 mL min^{-1} at the anode, while at the cathode, oxygen as an oxidant was used.

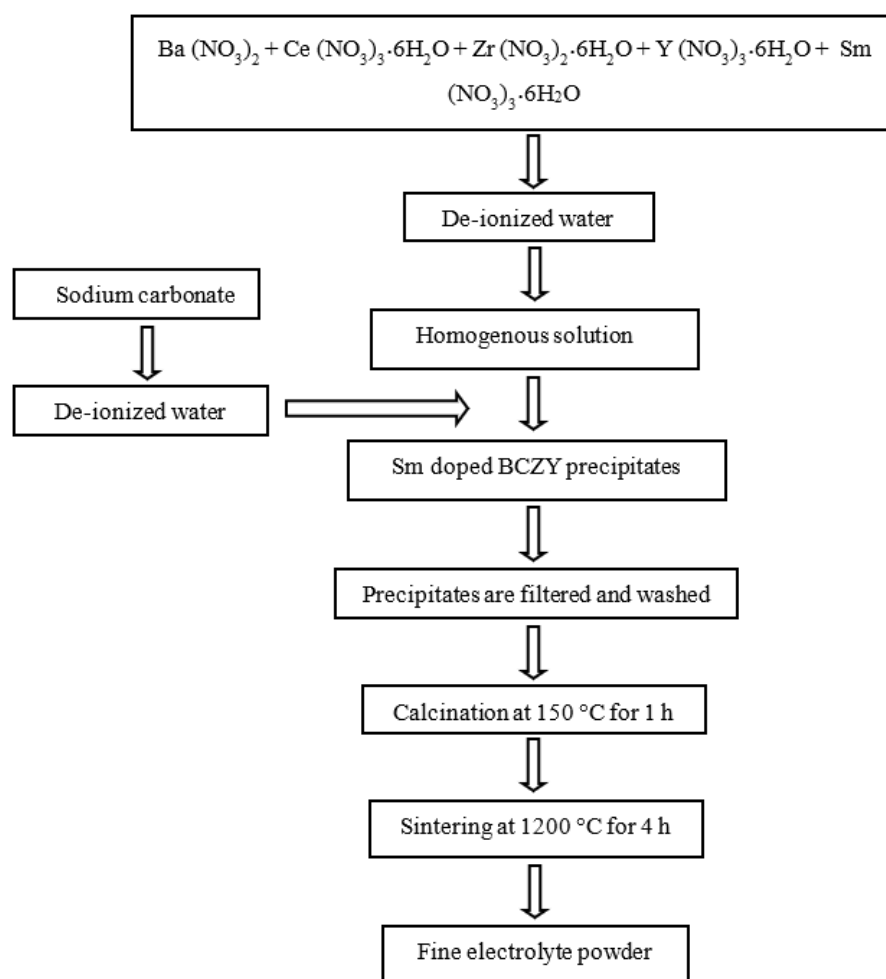


Figure 1. Flowchart of BaCe_{0.7-x}Sm_xZr_{0.2}Y_{0.1}O_{3-δ} synthesis by coprecipitation method.

3. Results

3.1. Structural Analysis

The XRD spectra of the BaCe_{0.7-x}Sm_xZr_{0.2}Y_{0.1}O_{3-δ} in the 2θ range, $20\text{--}70^\circ$, are shown in Figure 2. The Bragg peaks (002), (200), (213), (004), (220), and (611) correspond to the cubic perovskite structure (JCPDS card no. 34-0394). The secondary peak of Sm₂O₃ was observed for composition $x = 0.3$. The presence of a secondary peak can be attributed to the low sintering temperature which can be eliminated if the sintering temperature is increased to $>1400^\circ\text{C}$ [24]. The formation of Sm₂O₃ was due to the lattice expansion produced from the high doping concentration of Sm because SmO₂ diffuses into the CeO₂. The presence of the second phase can also be attributed to the fact that lanthanides occupy the A-site in the perovskite structure, and the solubility of the samarium ion that occupied the A-site is large because of the small ionic radii difference between Sm³⁺ (1.08 Å) and Ce⁴⁺ (0.97 Å). Moreover, doping of Sm ions substituted the Ce ions and caused volume expansion [28]. This volume change may also occur because of the mismatched ionic radii of the host and the dopant material [23,29].

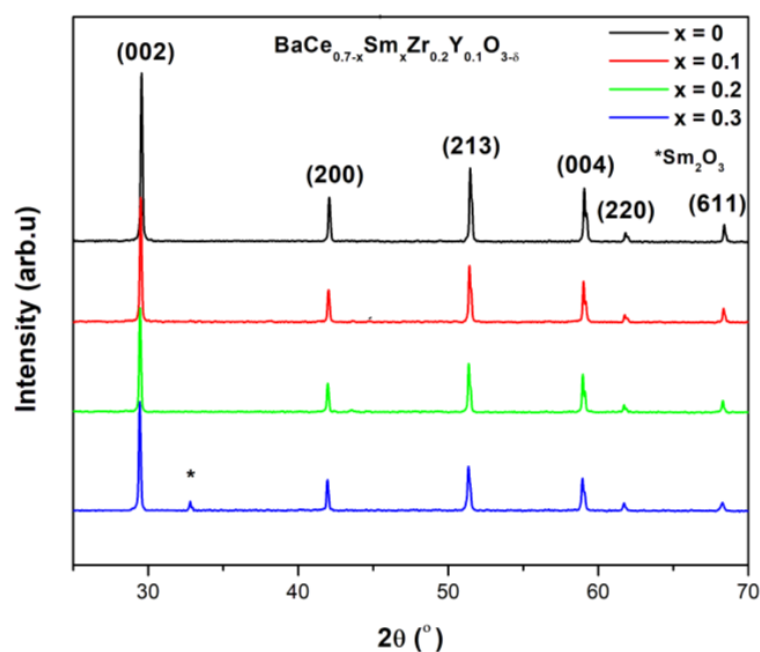


Figure 2. X-ray diffraction patterns of $\text{BaCe}_{0.7-x}\text{Sm}_x\text{Zr}_{0.2}\text{Y}_{0.1}\text{O}_{3-\delta}$.

The magnified (002) peaks for all the prepared compositions of $\text{BaCe}_{0.7-x}\text{Sm}_x\text{Zr}_{0.2}\text{Y}_{0.1}\text{O}_{3-\delta}$ are shown in Figure 3. The peak shifted at lower angles that can be attributed to the mismatched ionic radii of Sm (1.08 Å) and Ce (0.97 Å) within the perovskite structure, which resulted in lattice expansion [30]. It is also clear from the spectra that some BaCeO_3 planes exhibited low intensity, thus showing its low degree of crystallinity, which can be attributed to the fact that BaCeO_3 has not reacted fully because of insufficient energy with the host ceria lattice.

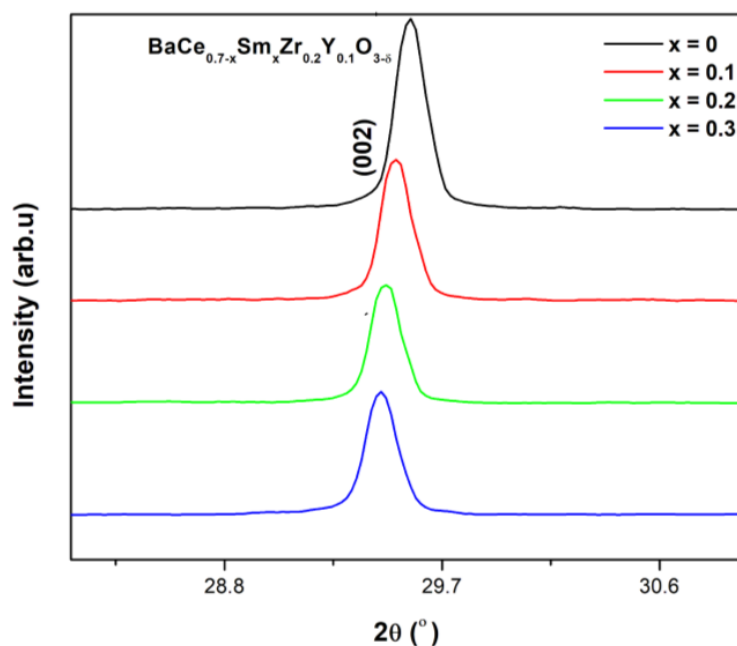


Figure 3. Peak (002) shifting of $\text{BaCe}_{0.7-x}\text{Sm}_x\text{Zr}_{0.2}\text{Y}_{0.1}\text{O}_{3-\delta}$ by Sm doping.

The crystallite size is calculated by the Scherrer formula [31]:

$$D = \frac{K\lambda}{\beta \cos \theta} \quad (1)$$

where K , λ , β , and θ represent the shape factor (0.94), the wavelength of the X-ray (0.154 nm), full width at half maximum (FWHM), and the diffraction angle, respectively. The crystallite sizes of $\text{BaCe}_{0.7-x}\text{Sm}_x\text{Zr}_{0.2}\text{Y}_{0.1}\text{O}_{3-\delta}$ are given in Table 1, and an increased crystallite size with an increased Sm concentration in $\text{BaCe}_{0.7-x}\text{Sm}_x\text{Zr}_{0.2}\text{Y}_{0.1}\text{O}_{3-\delta}$ can be observed [32].

Table 1. Crystallite size of $\text{BaCe}_{0.7-x}\text{Sm}_x\text{Zr}_{0.2}\text{Y}_{0.1}\text{O}_{3-\delta}$ compositions with $x = 0, 0.1, 0.2, 0.3$.

Material	Crystallite Size (nm)
$\text{BaCe}_{0.7}\text{Zr}_{0.2}\text{Y}_{0.1}\text{O}_{3-\delta}$	11
$\text{BaCe}_{0.6}\text{Sm}_{0.1}\text{Zr}_{0.2}\text{Y}_{0.1}\text{O}_{3-\delta}$	14
$\text{BaCe}_{0.5}\text{Sm}_{0.2}\text{Zr}_{0.2}\text{Y}_{0.1}\text{O}_{3-\delta}$	15
$\text{BaCe}_{0.4}\text{Sm}_{0.3}\text{Zr}_{0.2}\text{Y}_{0.1}\text{O}_{3-\delta}$	23

3.2. Surface Morphology

Figure 4 shows the SEM micrographs of the $\text{BaCe}_{0.7-x}\text{Sm}_x\text{Zr}_{0.2}\text{Y}_{0.1}\text{O}_{3-\delta}$ electrolyte materials. Each sample exhibited a different microstructure because of the varying concentrations of Sm. It is well-known that a porous electrolyte is not suitable for charge carrier transportation because an airtight structure is needed to avoid gas diffusion [33]. In the SEM micrographs, it can be seen that a dense structure is present for all the samples, thus making them suitable as an electrolyte.

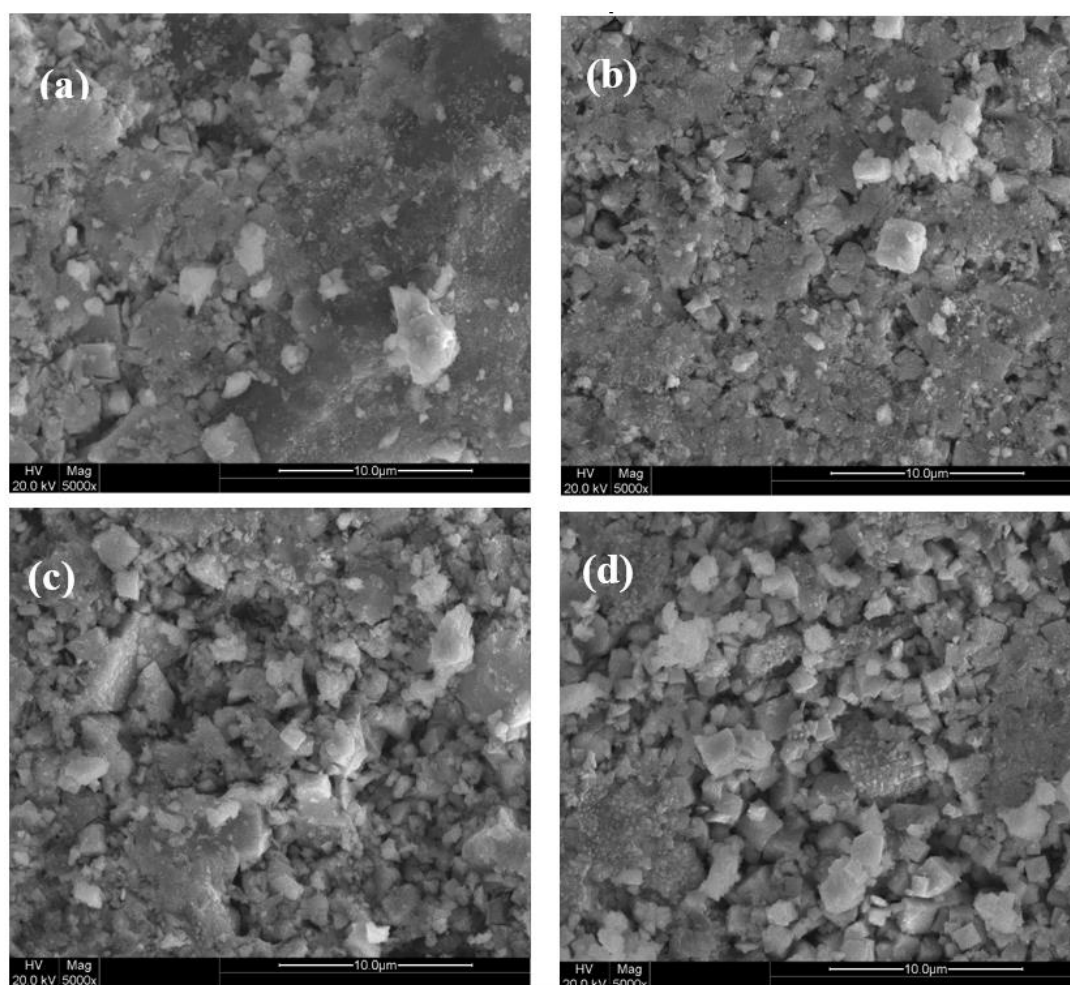


Figure 4. SEM analysis and the surface morphology of $\text{BaCe}_{0.7-x}\text{Sm}_x\text{Zr}_{0.2}\text{Y}_{0.1}\text{O}_{3-\delta}$ for $x = 0$ (a); $x = 0.1$ (b); $x = 0.2$ (c); and $x = 0.3$ (d).

Figure 4a represents the surface morphology of the $\text{BaCe}_{0.7-x}\text{Sm}_x\text{Zr}_{0.2}\text{Y}_{0.1}\text{O}_{3-\delta}$ ($x = 0$) perovskite electrolyte. It can be observed from the micrographs that this composition exhibits a more compact and denser structure compared to other compositions. Figure 4b–d represent the surface morphologies of the $\text{BaCe}_{0.7-x}\text{Sm}_x\text{Zr}_{0.2}\text{Y}_{0.1}\text{O}_{3-\delta}$ compositions. It is evident from the micrographs that the density of materials decreased with an increased content of Sm. Furthermore, crystal growth became more prominent with increased Sm doping. The effect of increased Sm doping not only slightly decreased the overall structure's compactness, but also increased the crystal growth. The crystallite size, calculated from the Scherrer equation, confirmed that the crystallite size increased with Sm doping. The increased compactness of $\text{BaCe}_{0.7-x}\text{Sm}_x\text{Zr}_{0.2}\text{Y}_{0.1}\text{O}_{3-\delta}$ with more concentration of Sm can be attributed to the fact that, for higher contents of samarium, the agglomeration of particles is large, making the structure less compact. It is also known that a higher Sm content is favorable for crystal growth, which is evident from the micrographs in Figure 4b–d [9,34]. The least compact structure was observed for the sample having a high content of Sm, that is, $\text{BaCe}_{0.7-x}\text{Sm}_x\text{Zr}_{0.2}\text{Y}_{0.1}\text{O}_{3-\delta}$ ($x = 0.3$).

3.3. FTIR Analysis

FTIR spectra of the $\text{BaCe}_{0.7-x}\text{Sm}_x\text{Zr}_{0.2}\text{Y}_{0.1}\text{O}_{3-\delta}$ electrolyte materials in the range of $4000\text{--}600\text{ cm}^{-1}$ are presented in Figure 5. The peaks, at 1423 cm^{-1} and 1413 cm^{-1} , represent O–H bending and show symmetrical disturbances in the $\text{BaCe}_{0.7-x}\text{Sm}_x\text{Zr}_{0.2}\text{Y}_{0.1}\text{O}_{3-\delta}$ ($x = 0.1\text{--}0.3$) electrolyte materials. The presence of a small O–H stretching mode is attributed to the hydroxyl group because of the ambient moisture. Small weight loss is noticeable in the further thermal analysis (Figure 7), which confirms the fact that moisture was present within the sample because of the humid environment. TGA analysis was done after sintering and, still, there was a small weight loss ($\sim 2.3\%$) up to 150°C . The absence of the sharp peak confirms the evaporation of adsorbed water completely already during the calcination and the sintering processes, and no prominent O–H stretching was present in the FTIR [35].

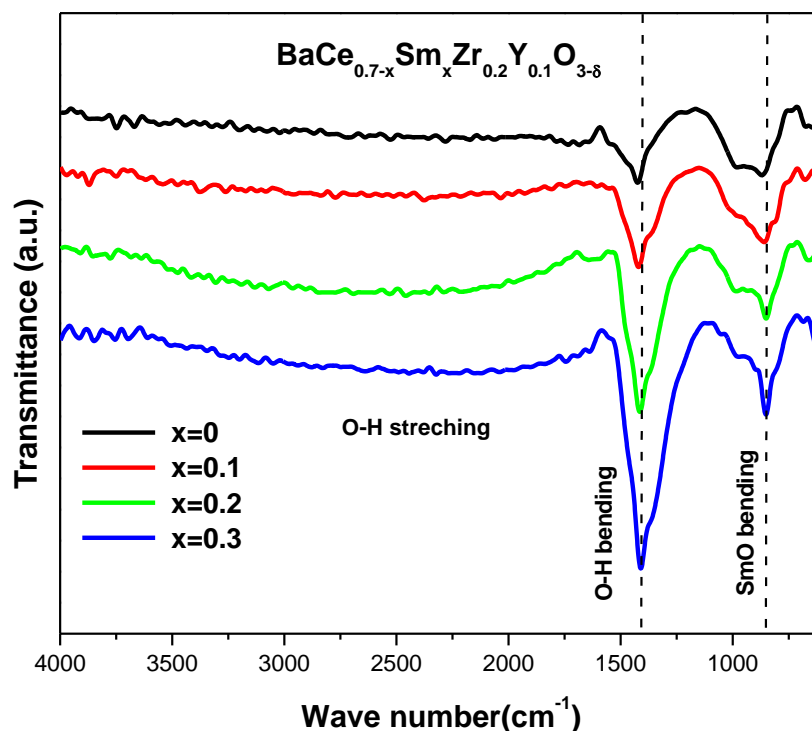


Figure 5. Fourier transform infrared spectra of $\text{BaCe}_{0.7-x}\text{Sm}_x\text{Zr}_{0.2}\text{Y}_{0.1}\text{O}_{3-\delta}$.

The peaks between 900 cm^{-1} and 800 cm^{-1} indicate M–O (M = metal) stretching modes. The perovskite structure was confirmed by peaks present around 700 cm^{-1} to 650 cm^{-1} and can be linked to the vibration of the B-site cations [36]. It is also clear that the intensity of peaks increases with an increase in the content of Sm because the high ratio of Sm in $\text{BaCe}_{0.7-x}\text{Sm}_x\text{Zr}_{0.2}\text{Y}_{0.1}\text{O}_{3-\delta}$ produces high structural symmetrical disturbances.

Figure 6 shows the magnified region of the FTIR spectra for the wavelength range of $650\text{--}1500\text{ cm}^{-1}$. Peak shifting is associated with the increased Sm concentration. Furthermore, this produces stretching and defects in the lattice structure. These variations develop the trapping effects of the charges between the dopant and the host [37]. The Ce–O bond length between the molecules decreases because of the difference in the electronegativity of neighboring atoms. The decrease in the Ce–O bond length shifts the peak towards the lower wavenumber. In $\text{BaCe}_{0.7-x}\text{Sm}_x\text{Zr}_{0.2}\text{Y}_{0.1}\text{O}_{3-\delta}$, the stretching is also produced because of the increased Sm concentration, which means a decrease in the Ce–O bond [28].

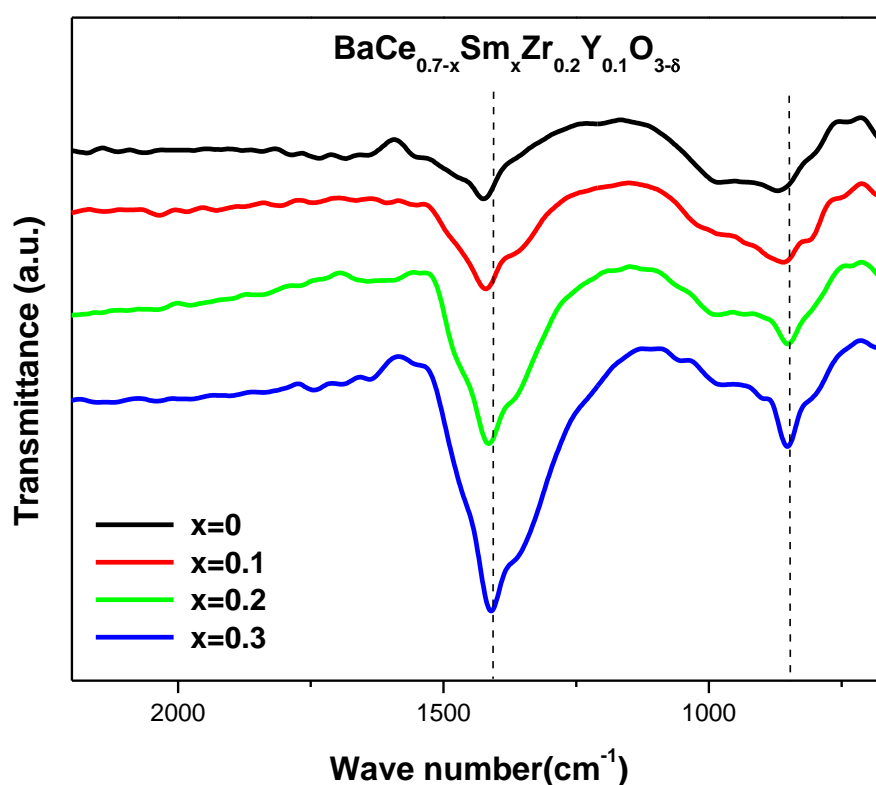


Figure 6. Peak shifts in the magnified FTIR spectra of $\text{BaCe}_{0.7-x}\text{Sm}_x\text{Zr}_{0.2}\text{Y}_{0.1}\text{O}_{3-\delta}$.

The high symmetrical disturbance observed through the FTIR is also confirmed by the Goldschmidt tolerance factor. The high symmetrical disturbance means highly distorted symmetry that results because of Sm doping at the B-site to create more oxygen vacancies. The perfect ABO_3 perovskites (A = Ca, Ba, Sr; B = Ce, Zr) have low oxygen vacancies and, therefore, have low proton conduction. The B site doping can increase the oxygen vacancies because of the charge compensation associated with higher structural distortion [14].

The Goldschmidt tolerance factor (t) is a broadly accepted criterion of the perovskite structure, and an ideal cubic perovskite structure has $t = 1$. However, many perovskite materials deviate from the ideal structure and exhibit disordered structures. The value of the tolerance factor calculated for the doped $\text{BaCe}_{0.7-x}\text{Sm}_x\text{Zr}_{0.2}\text{Y}_{0.1}\text{O}_{3-\delta}$ electrolyte is 1.01, showing that Sm-doped $\text{BaCe}_{0.7-x}\text{Sm}_x\text{Zr}_{0.2}\text{Y}_{0.1}\text{O}_{3-\delta}$ retained the perovskite structure, but with tensile A–O bond and a compressive B–O bond due to the displacement of the B-site cations within the BO_6 octahedra, which resulted in distorted structural symmetry, as has been reported in the literature [14]. The value also shows that the perovskite structure obtained is cubic.

3.4. Thermal Analysis

The TGA curves recorded for the sintered $\text{BaCe}_{0.7-x}\text{Sm}_x\text{Zr}_{0.2}\text{Y}_{0.1}\text{O}_{3-\delta}$ materials are shown in Figure 7. The curves are divided into two regions. Region I and Region II correspond to 30–150 °C and 150–900 °C, respectively. A small weight loss of nearly 2.3% occurred only in Region I and can be attributed to the evaporation of the adsorbed water within the samples because of the ambient moisture [38]. In the range between 150–900 °C, there was no major weight loss, as indicated by the constant curve, since all the organic compounds were already decomposed/evaporated during the sintering process. Furthermore, thermal testing reveals that no chemical reaction occurred in the IT-SOFC in this temperature range [39].

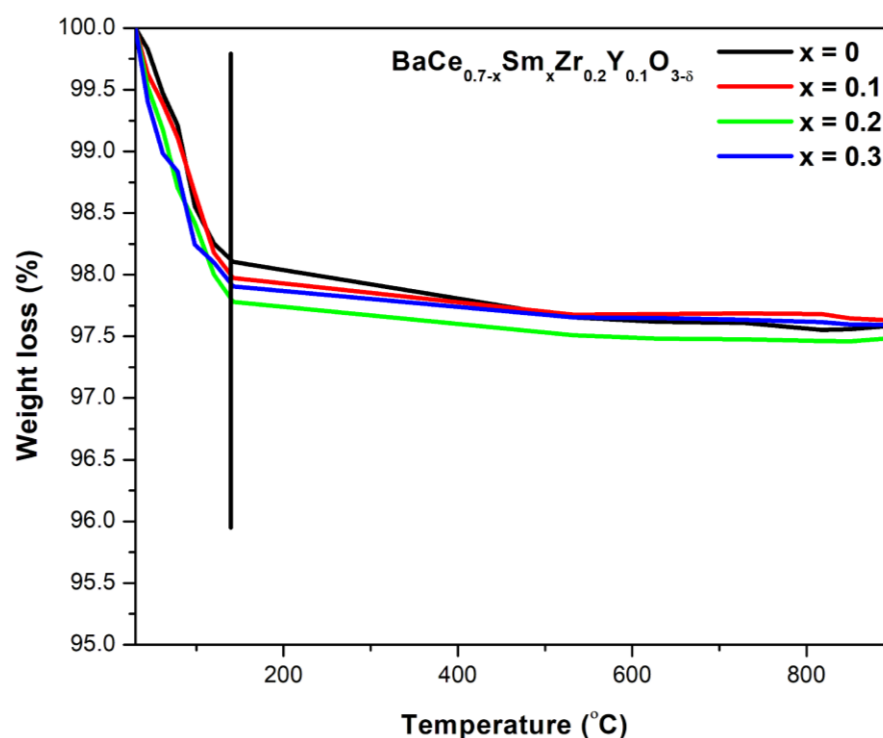


Figure 7. TGA curves of postsintered $\text{BaCe}_{0.7-x}\text{Sm}_x\text{Zr}_{0.2}\text{Y}_{0.1}\text{O}_{3-\delta}$ electrolyte materials.

3.5. Ionic Conductivity

The ionic conductivity of the $\text{BaCe}_{0.7-x}\text{Sm}_x\text{Zr}_{0.2}\text{Y}_{0.1}\text{O}_{3-\delta}$ materials was measured in fuel cell condition, i.e., wet H_2 was supplied to the one surface of the electrolyte, while the other surface was supplied air. Figure 8 shows the Arrhenius plot as a function of temperature for all the compositions of $\text{BaCe}_{0.7-x}\text{Sm}_x\text{Zr}_{0.2}\text{Y}_{0.1}\text{O}_{3-\delta}$. The conductivity, based on the Arrhenius equation, is [40]:

$$\sigma = \frac{A}{T} \exp\left(-\frac{E_a}{KT}\right) \quad (2)$$

where σ , A , E_a , k , and T are the conductivity, the material-dependent constant, the activation energy, the Boltzmann constant, and the absolute temperature, respectively. The mobility and concentration of charge carriers strongly effects the conductivity. It is well-known that, by an increase in concentration, the number of charge carriers increases and, hence, mobility increases. Moreover, the charge carriers number and their mobility depend on the pre-exponential factor and the hopping activation energy [41].

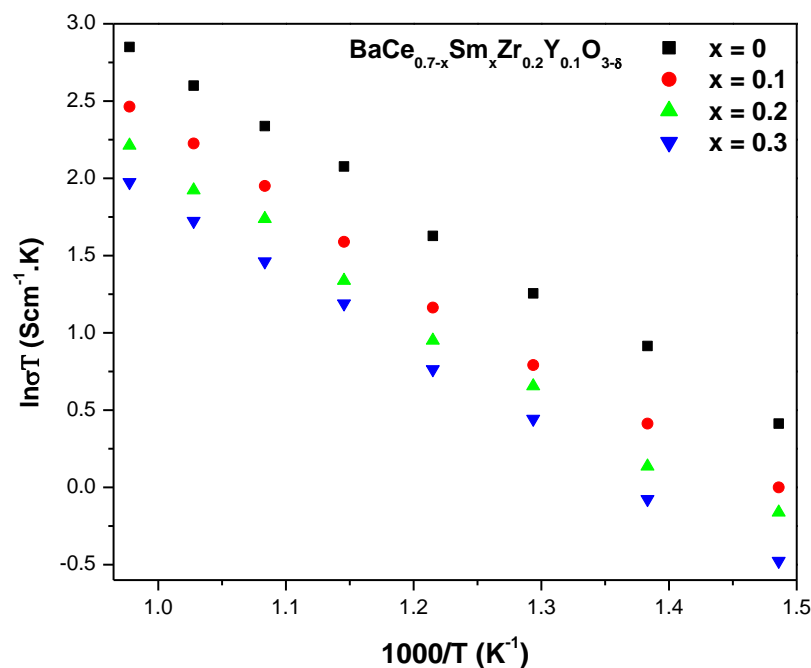


Figure 8. The Arrhenius plot represents the conductivity of $\text{BaCe}_{0.7-x}\text{Sm}_x\text{Zr}_{0.2}\text{Y}_{0.1}\text{O}_{3-\delta}$ as a function of temperature.

It can be observed from the Arrhenius plot that $\text{BaCe}_{0.7-x}\text{Sm}_x\text{Zr}_{0.2}\text{Y}_{0.1}\text{O}_{3-\delta}$ ($x = 0$) exhibits higher conductivity compared to Sm-doped $\text{BaCe}_{0.7-x}\text{Sm}_x\text{Zr}_{0.2}\text{Y}_{0.1}\text{O}_{3-\delta}$ compositions. The proton conductivity of the perovskite electrolyte increases because of the small trapping effects. Trapping effects are generally produced because of the symmetrical disturbance and defects in the lattice structure, as revealed by the FTIR analysis. Protonic conductivity also depends on the transport mechanism. In $\text{BaCe}_{0.7-x}\text{Sm}_x\text{Zr}_{0.2}\text{Y}_{0.1}\text{O}_{3-\delta}$ compositions, Sm gets doped at the Ce position because of the partitioning property of the lanthanide elements, which reduce the Ce ions and increase the trapping effects, therefore resulting in reduced conductivity [42,43]. Moreover, in perovskites, the structure bandwidth reduces by the distortion produced in the M–O–M bond and minimizes the mobility of the charge carriers between the host and guest metal sites. Therefore, in the current case, the distortion is increased by the increased concentration of Sm, also confirmed by FTIR. Hence, the lattice distortion raises the activation energy of the charge carriers. Moreover, the charge carriers depend on the pre-exponential factor, i.e. the concentration of available and occupied sites. A single occupied site depends on the energy gap, and the single available site depends upon the grain shape, controlled by the sintering conditions [44]. The obtained conductivity is comparable to the already reported values, but it can be further increased if the sintering temperature is greater than 1400 °C to crystallize the secondary phases. Thus, it can be concluded that the higher amount of Sm doping leads to the undesirable formation of the Sm_2O_3 phase because some Sm^{3+} ratio do not replaced the Ce^{4+} ions, which further decreases the ionic conductivity [10,45,46].

3.6. Electrochemical Performance

The electrochemical performances, evaluated at 600 °C, of four button cells having $\text{BaCe}_{0.7-x}\text{Sm}_x\text{Zr}_{0.2}\text{Y}_{0.1}\text{O}_{3-\delta}$ electrolyte materials are shown in Figure 9. The cell performance is strongly dependent on the microstructure, density, crystallite size, and conductivity [37]. The values of the conductivity of the $\text{BaCe}_{0.7-x}\text{Sm}_x\text{Zr}_{0.2}\text{Y}_{0.1}\text{O}_{3-\delta}$ materials show that it decreased with increased Sm content. As a result, the oxygen vacancies decreased [47]. The observed power densities of the $\text{BaCe}_{0.7-x}\text{Sm}_x\text{Zr}_{0.2}\text{Y}_{0.1}\text{O}_{3-\delta}$ electrolyte are 0.39, 0.35, 0.32, and 0.29 W cm^{-2} with an OCV of 1.0, 1.012, 1.017, and 1.02 V, respectively. The achieved high power density of $\text{BaCe}_{0.7-x}\text{Sm}_x\text{Zr}_{0.2}\text{Y}_{0.1}\text{O}_{3-\delta}$ ($x = 0$) can be explained as

high protonic conductivity, compared to other compositions, because the doping of Sm produced distortion in the M–O–M bond, as confirmed by FTIR.

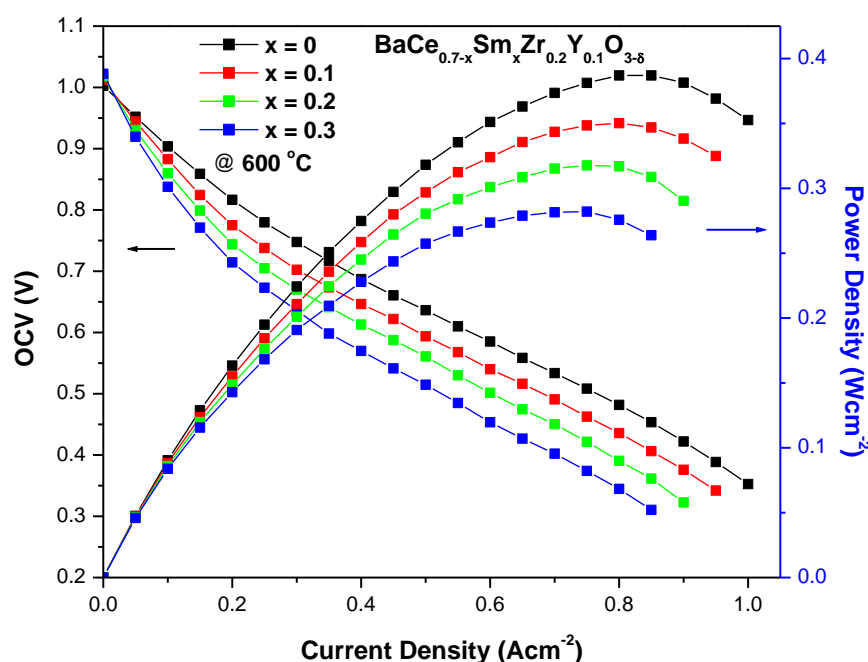


Figure 9. Electrochemical performance of the cells with $\text{BaCe}_{0.7-x}\text{Sm}_x\text{Zr}_{0.2}\text{Y}_{0.1}\text{O}_{3-\delta}$ as electrolyte at 600 °C.

The presence of the secondary phase of SmO_2 in $\text{BaCe}_{0.7-x}\text{Sm}_x\text{Zr}_{0.2}\text{Y}_{0.1}\text{O}_{3-\delta}$ ($x = 0.3$) also affected the cell performance because samarium belongs to the lanthanide group, having the property of partitioning from both the A-site and the B-site in perovskite structures. It is also reported that electron–hole conductivity in the oxidation environment can also reduce the OCV in proton-conducting electrolytes. Another factor that can affect the performance of the cell is the low sintering temperature (1200 °C), which results in a small TPB length, therefore causing a reduced electrochemical reaction at the TPB [25,36,48]. In the present case, the power density of 390 mW cm^{-2} at 600 °C for $\text{BaCe}_{0.7-x}\text{Sm}_x\text{Zr}_{0.2}\text{Y}_{0.1}\text{O}_{3-\delta}$ sintered at a low sintering temperature is better than the $300 (\text{mW cm}^{-2})$ at 550 °C for $\text{BaCe}_{0.5}\text{Zr}_{0.35}\text{Y}_{0.15}\text{O}_{3-\delta}$, which can be improved by sintering material at a high temperature [49].

Table 2 shows the reported power densities of cells having BCZY electrolytes, along with electrodes, fuel, operating temperatures, and OCVs.

Table 2. Power densities of SOFCs having BCZY electrolytes.

Electrolyte	Cathode	Anode	Fuel and Temperature	OCV (V)	Power Density (mW cm^{-2})
$\text{BaCe}_{0.5}\text{Zr}_{0.35}\text{Y}_{0.15}\text{O}_{3-\delta}$ [49]	LSC	Ni-BCZY	Humidified H_2 (~3% H_2O) (@550 °C)	1.01	300
$\text{BaZr}_{0.4}\text{Ce}_{0.4}\text{Y}_{0.2}\text{O}_{3-\delta}$ [50]	BSCF	Ni-BCZY	Humidified H_2 (~3% H_2O) (@600 °C)	0.9	360
$\text{BaCe}_{0.4}\text{Zr}_{0.4}\text{Y}_{0.2}\text{O}_{3-\delta}$ [51]	PrNi	Ni-BCZY	Humidified H_2 (~3% H_2O) (@550 °C)	1.05	63
$\text{BaZr}_{0.1}\text{Ce}_{0.7}\text{Y}_{0.2}\text{O}_{3-\delta}$ [25]	LSCF	Ni-BCZY	Humidified H_2 (~3% H_2O) (@600 °C)	1.05	477

4. Discussion

The XRD spectra reveal that the synthesized $\text{BaCe}_{0.7-x}\text{Sm}_x\text{Zr}_{0.2}\text{Y}_{0.1}\text{O}_{3-\delta}$ proton-conducting electrolyte retained a cubic perovskite structure. However, a secondary phase of Sm_2O_3 was observed for sample $x = 0.3$, which can be attributed to the lattice expansion produced by the high doping concentration of Sm. The magnified (002) plane confirmed that the peak shifted toward a lower angle with Sm doping, which resulted in lattice expansion because of mismatched ionic radii of Sm and Ce. The crystallite size, calculated by the Scherrer equation, shows that it increased with an increased Sm concentration, and ranged from 11–23 nm. SEM micrographs revealed that all samples had sufficient density to be utilized as an electrolyte in an SOFC. It was also observed that the compactness, or density, of the electrolyte decreased with increased Sm doping because a higher content of Sm favors the particle agglomeration that results in the decreased compactness of the structure. The FTIR spectra confirmed the presence of M–O stretching modes, along with high structural distortion due to Sm doping. Peak shifting was also observed, due to Sm doping, which created stretching and defects in the lattice structure. TGA analysis indicated a small weight loss (2.3%) up to 150 °C due to the evaporation of adsorbed water, and no weight loss was observed at high temperatures, showing that all samples were thermally stable at the SOFC operating temperature. An Arrhenius plot revealed that the conductivity of the $\text{BaCe}_{0.7-x}\text{Sm}_x\text{Zr}_{0.2}\text{Y}_{0.1}\text{O}_{3-\delta}$ decreased with an increased concentration of the Sm dopant because the increased content of Sm produced increased trapping effects, which resulted in decreased ionic conductivity. The electrochemical performance exhibited a peak power density of 390 mW cm^{-2} at 600 °C in humidified H_2 (3% H_2O).

5. Conclusions

Perovskite materials are of particular interest in numerous applications because of their exceptional properties. However, perovskite materials in their ideal structure have poor proton conductivity because of low oxygen vacancies and cannot be used as electrolytes in SOFCs. This project aimed to increase the oxygen vacancies in BaCeO_3 . Sm-doped $\text{BaCe}_{0.7-x}\text{Sm}_x\text{Zr}_{0.2}\text{Y}_{0.1}\text{O}_{3-\delta}$ proton-conducting electrolyte material was synthesized by the cost- and time-effective coprecipitation method. The structural and surface analyses of $\text{BaCe}_{0.7-x}\text{Sm}_x\text{Zr}_{0.2}\text{Y}_{0.1}\text{O}_{3-\delta}$ provided a cubic perovskite crystalline phase and a dense microstructure, respectively. A secondary Sm_2O_3 phase of $\text{BaCe}_{0.7-x}\text{Sm}_x\text{Zr}_{0.2}\text{Y}_{0.1}\text{O}_{3-\delta}$ was observed only for the composition with $x = 0.3$. Peak shifting in the FTIR investigations were observed, indicating the change in the bond length between metal and oxygen. Among all the prepared electrolytes, the performance of $\text{BaCe}_{0.7-x}\text{Sm}_x\text{Zr}_{0.2}\text{Y}_{0.1}\text{O}_{3-\delta}$ with the composition, $x = 0$, was at the top, with 0.39 W cm^{-2} . The power densities for the other electrolytes of $\text{BaCe}_{0.7-x}\text{Sm}_x\text{Zr}_{0.2}\text{Y}_{0.1}\text{O}_{3-\delta}$, with $x = 0.1, 0.2$, and 0.3 were achieved as $0.35, 0.32$, and 0.29 W cm^{-2} , respectively. The doping of Zr and Y increased the oxygen vacancies, along with structural defects, which resulted in the increased performance of the cell. The doping of the Sm within $\text{BaCe}_{0.7-x}\text{Sm}_x\text{Zr}_{0.2}\text{Y}_{0.1}\text{O}_{3-\delta}$, on the other hand, produced more oxygen vacancies but also increased the trapping effects within the structure because of the partitioning property of the lanthanide elements that leads to a reduced performance, compared to $\text{BaCe}_{0.7-x}\text{Zr}_{0.2}\text{Y}_{0.1}\text{O}_{3-\delta}$. The overall performance of all cells having the perovskite electrolyte, $\text{BaCe}_{0.7-x}\text{Sm}_x\text{Zr}_{0.2}\text{Y}_{0.1}\text{O}_{3-\delta}$, shows that all compositions can be used as proton-conducting electrolytes for IT-SOFCs. Furthermore, it is concluded that the coprecipitation synthesis route is a suitable and cost-effective method for synthesizing $\text{BaCe}_{0.7-x}\text{Sm}_x\text{Zr}_{0.2}\text{Y}_{0.1}\text{O}_{3-\delta}$ perovskite electrolyte material.

Author Contributions: Conceptualization: M.I., Data curation: M.R., A.N.T., Q.t.A., Formal analysis: M.I., A.N.T., A.G., R.R., M.A., K.S., M.R., Investigation: M.I., M.K., A.G., R.R., M.A., Q.t.A. Methodology: M.I., A.N.T., M.K., A.G., M.R. Project administration: M.I., Resources: M.I., A.S., Software: A.N.T., Supervision: M.I., Validation: M.I., M.K., A.S., Writing—original draft: M.I., M.K., Writing—review & editing: M.I., A.N.T., K.S., A.G., R.R., M.A., Q.u.A. All authors have read and agreed to the published version of the manuscript.

Funding: The current project is completed without any local or foreign funding resources.

Institutional Review Board Statement: Not applicable.

Informed Consent Statement: Not applicable.

Data Availability Statement: The data presented in this study are available on request from the corresponding author.

Acknowledgments: The authors acknowledge the support of Department of Physics, UET, Lahore, Pakistan, for completion of current project.

Conflicts of Interest: The authors declare no conflict of interest.

References

1. Tan, L.; Dong, X.; Chen, C.; Gong, Z.; Wang, M. Diverse system layouts promising fine performance demonstration: A comprehensive review on present designs of SOFC-based energy systems for building applications. *Energy Convers. Manag.* **2021**, *245*, 114539. [\[CrossRef\]](#)
2. Irshad, M.; Khalid, M.; Rafique, M.; Ahmad, N.; Siraj, K.; Raza, R.; Sadiq, M.; Ahsan, M.; Ghaffar, A.; Ashfaq, A. Evaluation of $\text{BaCo}_{0.4}\text{Fe}_{0.4}\text{Zr}_{0.2-x}\text{Ni}_x\text{O}_{3-\delta}$ perovskite cathode using nickel as a sintering aid for IT-SOFC. *RSC Adv.* **2021**, *11*, 14475–14483. [\[CrossRef\]](#)
3. Cimen, F.M.; Kumuk, B.; Ilbas, M. Simulation of hydrogen and coal gas fueled flat-tubular solid oxide fuel cell (FT-SOFC). *Int. J. Hydrogen Energy* **2021**, in press. [\[CrossRef\]](#)
4. Liu, F.; Duan, C. Direct-hydrocarbon proton-conducting solid oxide fuel cells. *Sustainability* **2021**, *13*, 4736. [\[CrossRef\]](#)
5. Irshad, M.; Idrees, R.; Siraj, K.; Shakir, I.; Rafique, M.; Ain, Q.U.; Raza, R. Electrochemical evaluation of mixed ionic electronic perovskite cathode $\text{LaNi}_{1-x}\text{Co}_x\text{O}_{3-\delta}$ for IT-SOFC synthesized by high temperature decomposition. *Int. J. Hydrogen Energy* **2021**, *46*, 10448–10456. [\[CrossRef\]](#)
6. Fu, Q.; Li, Z.; Wei, W.; Liu, F.; Xu, X.; Liu, Z. Performance enhancement of planar solid oxide fuel cell using a novel interconnector design. *Int. J. Hydrogen Energy* **2021**, *46*, 21634–21656. [\[CrossRef\]](#)
7. Ahsan, M.; Irshad, M.; Fu, P.F.; Siraj, K.; Raza, R.; Javed, F. The effect of calcination temperature on the properties of Ni-SDC cermet anode. *Ceram. Int.* **2020**, *46*, 2780–2785. [\[CrossRef\]](#)
8. Irshad, M.; Siraj, K.; Raza, R.; Javed, F.; Ahsan, M.; Shakir, I.; Rafique, M.S. High performance of SDC and GDC core shell type composite electrolytes using methane as a fuel for low temperature SOFC. *AIP Adv.* **2016**, *6*, 025202. [\[CrossRef\]](#)
9. Maffucci, A.; Maksimenko, S.A. (Eds.) *Fundamental and Applied Nano-Electromagnetics II*, 1st ed.; NATO Science for Peace and Security Series B: Physics and Biophysics; Springer: Dordrecht, The Netherlands, 2019; ISBN 978-94-024-1686-2.
10. Irshad, M.; Siraj, K.; Raza, R.; Ali, A.; Tiwari, P.; Zhu, B.; Rafique, A.; Ali, A.; Ullah, M.K.; Usman, A. A brief description of high temperature solid oxide fuel cell's operation, materials, design, fabrication technologies and performance. *Appl. Sci.* **2016**, *6*, 75. [\[CrossRef\]](#)
11. Wilberforce, T.; Olabi, A.G. Performance prediction of proton exchange membrane fuel cells (PEMFC) using adaptive neuro inference system (ANFIS). *Sustainability* **2020**, *12*, 4952. [\[CrossRef\]](#)
12. Sunarso, J.; Hashim, S.S.; Zhu, N.; Zhou, W. Perovskite oxides applications in high temperature oxygen separation, solid oxide fuel cell and membrane reactor: A review. *Prog. Energy Combust. Sci.* **2017**, *61*, 57–77. [\[CrossRef\]](#)
13. Cao, J.; Su, C.; Ji, Y.; Yang, G.; Shao, Z. Recent advances and perspectives of fluorite and perovskite-based dual-ion conducting solid oxide fuel cells. *J. Energy Chem.* **2021**, *57*, 406–427. [\[CrossRef\]](#)
14. Li, S.; Irvine, J.T.S. Non-stoichiometry, structure and properties of proton-conducting perovskite oxides. *Solid State Ion.* **2021**, *361*, 115571. [\[CrossRef\]](#)
15. Hossain, S.; Abdalla, A.M.; Jamain, S.N.B.; Zaini, J.; Azad, A. A review on proton conducting electrolytes for clean energy and intermediate temperature-solid oxide fuel cells. *Renew. Sustain. Energy Rev.* **2017**, *79*, 750–764. [\[CrossRef\]](#)
16. Irshad, M.; Siraj, K.; Raza, R.; Rafique, M.; Usman, M.; Ain, Q.U.; Ghaffar, A. Evaluation of densification effects on the properties of 8 mol % yttria stabilized zirconia electrolyte synthesized by cost effective coprecipitation route. *Ceram. Int.* **2021**, *47*, 2857–2863. [\[CrossRef\]](#)
17. Koteswararao, P.; Suresh, B.M.; Wani, B.; Rao, P. Review on different components of solid oxide fuel cells. *J. Powder Metall. Min.* **2017**, *6*, 181. [\[CrossRef\]](#)
18. Sawant, P.; Varma, S.; Wani, B.; Bharadwaj, S. Synthesis, stability and conductivity of $\text{BaCe}_{0.8-x}\text{Zr}_x\text{Y}_{0.2}\text{O}_{3-\delta}$ as electrolyte for proton conducting SOFC. *Int. J. Hydrogen Energy* **2012**, *37*, 3848–3856. [\[CrossRef\]](#)
19. Ogawa, T.; Takeuchi, M.; Kajikawa, Y. Comprehensive analysis of trends and emerging technologies in all types of fuel cells based on a computational method. *Sustainability* **2018**, *10*, 458. [\[CrossRef\]](#)
20. Han, D.; Shinoda, K.; Sato, S.; Majima, M.; Uda, T. Correlation between electroconductive and structural properties of proton conductive acceptor-doped barium zirconate. *J. Mater. Chem. A* **2015**, *3*, 1243–1250. [\[CrossRef\]](#)
21. Imashuku, S.; Uda, T.; Nose, Y.; Taniguchi, G.; Ito, Y.; Awakura, Y. Dependence of dopant cations on microstructure and proton conductivity of barium zirconate. *J. Electrochem. Soc.* **2009**, *156*, B1. [\[CrossRef\]](#)

22. Meng, Y.; Gao, J.; Huang, H.; Zou, M.; Duffy, J.; Tong, J.; Brinkman, K.S. A high-performance reversible protonic ceramic electrochemical cell based on a novel Sm-doped BaCe_{0.7}Zr_{0.1}Y_{0.2}O_{3-δ} electrolyte. *J. Power Sources* **2019**, *439*, 227093. [\[CrossRef\]](#)
23. Usman, M.; Saqib, S.; Zubair, S.W.H.; Irshad, M.; Kazmi, A.H.; Noor, A.; Zaman, H.U.; Nasir, Z.; Malik, M.A.I. Experimental assessment of regenerated lube oil in spark-ignition engine for sustainable environment. *Adv. Mech. Eng.* **2020**, *12*, 1–10. [\[CrossRef\]](#)
24. Shi, Z.; Sun, W.; Wang, Z.; Qian, J.; Liu, W. Samarium and yttrium codoped BaCeO₃ proton conductor with improved sinterability and higher electrical conductivity. *ACS Appl. Mater. Interfaces* **2014**, *6*, 5175–5182. [\[CrossRef\]](#) [\[PubMed\]](#)
25. Lee, K.-R.; Tseng, C.-J.; Jang, S.-C.; Lin, J.-C.; Wang, K.-W.; Chang, J.-K.; Chen, T.-C.; Lee, S.-W. Fabrication of anode-supported thin BCZY electrolyte protonic fuel cells using NiO sintering aid. *Int. J. Hydrogen Energy* **2019**, *44*, 23784–23792. [\[CrossRef\]](#)
26. Liu, Z.; Chen, M.; Zhou, M.; Cao, D.; Liu, P.; Wang, W.; Liu, M.; Huang, J.; Shao, J.; Liu, J. Multiple effects of iron and nickel additives on the properties of proton conducting yttrium-doped barium cerate-zirconate electrolytes for high-performance solid oxide fuel cells. *ACS Appl. Mater. Interfaces* **2020**, *12*, 50433–50445. [\[CrossRef\]](#) [\[PubMed\]](#)
27. Hanifi, A.R.; Sandhu, N.K.; Etsell, T.H.; Luo, J.-L.; Sarkar, P. Fabrication and characterization of a tubular ceramic fuel cell based on BaZr_{0.1}Ce_{0.7}Y_{0.1}Yb_{0.1}O_{3-δ} proton conducting electrolyte. *J. Power Sources* **2017**, *341*, 264–269. [\[CrossRef\]](#)
28. Zhang, C.; Zhao, H.; Zhai, S. Electrical conduction behavior of proton conductor BaCe_{1-x}Sm_xO_{3-δ} in the intermediate temperature range. *Int. J. Hydrogen Energy* **2011**, *36*, 3649–3657. [\[CrossRef\]](#)
29. Iwahara, H.; Uchida, H.; Morimoto, K. High temperature solid electrolyte fuel cells using perovskite-type oxide based on BaCeO [sub 3]. *J. Electrochem. Soc.* **1990**, *137*, 462–465. [\[CrossRef\]](#)
30. Lu, X.; Ding, Y.; Chen, Y. Ba_{0.5}Sr_{0.5}Zn_{0.2}Fe_{0.8}O_{3-δ}–BaCe_{0.5}Zr_{0.3}Y_{0.16}Zn_{0.04}O_{3-δ} composite cathode for proton-conducting solid oxide fuel cells. *J. Alloys Compd.* **2009**, *484*, 856–859. [\[CrossRef\]](#)
31. Ravel, B.; Newville, M. ATHENA, ARTEMIS, HEPHAESTUS: Data analysis for X-ray absorption spectroscopy using IFEFFIT. *J. Synchrotron Radiat.* **2005**, *12*, 537–541. [\[CrossRef\]](#)
32. Yamazaki, Y.; Sánchez, R.H.; Haile, S.M. High total proton conductivity in large-grained yttrium-doped barium zirconate. *Chem. Mater.* **2009**, *21*, 2755–2762. [\[CrossRef\]](#)
33. Aygün, B.; Özdemir, H.; Öksüzömer, M.F. Structural, morphological and conductivity properties of samaria doped ceria (Sm_xCe_{1-x}O_{2-x/2}) electrolytes synthesized by electrospinning method. *Mater. Chem. Phys.* **2019**, *232*, 82–87. [\[CrossRef\]](#)
34. Inaba, H.; Tagawa, H. Ceria-based solid electrolytes. *Solid State Ion.* **1996**, *83*, 1–16. [\[CrossRef\]](#)
35. Irshad, M.; Ain, Q.; Siraj, K.; Raza, R.; Tabish, A.N.; Rafique, M.; Idrees, R.; Khan, F.; Majeed, S.; Ahsan, M. Evaluation of BaZr_{0.8}X_{0.2} (X = Y, Gd, Sm) proton conducting electrolytes sintered at low temperature for IT-SOFC synthesized by cost effective combustion method. *J. Alloys Compd.* **2020**, *815*, 152389. [\[CrossRef\]](#)
36. Njoku, C.B.; Ndungu, P.G. Synthesis and characterization of novel Ce_{0.8}Sm_{0.2}Fe_{0.9}Ir_{0.03}Co_{0.07}O_{3-δ} perovskite material and possible application as a cathode for low-intermediate temperature SOFCs. *Mater. Res. Bull.* **2015**, *68*, 100–108. [\[CrossRef\]](#)
37. Tariq, S.; Marium, A.; Raza, R.; Ahmad, M.A.; Khan, M.A.; Abbas, G.; Boota, M.W.; Imran, S.K.; Arshad, S.; Ikram, M. Comparative study of Ce_{0.8}Sm_{0.2}Ba_{0.8}O_{3-δ} (YB-SDC) electrolyte by various chemical synthesis routes. *Results Phys.* **2018**, *8*, 780–784. [\[CrossRef\]](#)
38. Gonçalves, M.; Maram, P.S.; Navrotsky, A.; Muccillo, R. Effect of synthesis atmosphere on the proton conductivity of Y-doped barium zirconate solid electrolytes. *Ceram. Int.* **2016**, *42*, 13689–13696. [\[CrossRef\]](#)
39. Muccillo, R.; Muccillo, E.N.S.; Andrade, T.F.; Oliveira, O.R. Thermal analyses of yttrium-doped barium zirconate with phosphor pentoxide, boron oxide and zinc oxide addition. *J. Therm. Anal. Calorim.* **2017**, *130*, 1791–1799. [\[CrossRef\]](#)
40. Uthayakumar, A.; Pandiyan, A.; Moorthy, S.B. K Yttrium dependent space charge effect on modulating the conductivity of barium zirconate electrolyte for solid oxide fuel cell. *Int. J. Hydrogen Energy* **2018**, *43*, 23488–23499. [\[CrossRef\]](#)
41. Han, D.; Shinoda, K.; Uda, T. Dopant site occupancy and chemical expansion in rare earth-doped barium zirconate. *J. Am. Ceram. Soc.* **2013**, *97*, 643–650. [\[CrossRef\]](#)
42. Madhavan, B.; Ashok, A. Review on nanoperovskites: Materials, synthesis, and applications for proton and oxide ion conductivity. *Ionics* **2015**, *21*, 601–610. [\[CrossRef\]](#)
43. Seeharaj, P.; Charoonsuk, T.; Pasupong, P.; Kim-Lohsoontorn, P.; Vittayakorn, N. Phase formation, microstructure, and densification of yttrium-doped barium zirconate prepared by the sonochemical method. *Int. J. Appl. Ceram. Technol.* **2015**, *13*, 200–208. [\[CrossRef\]](#)
44. Yun, D.S.; Kim, J.; Kim, S.-J.; Lee, J.-H.; Kim, J.-N.; Yoon, H.C.; Yu, J.H.; Kwak, M.; Yoon, H.; Cho, Y.; et al. Structural and electrochemical properties of dense yttria-doped barium zirconate prepared by solid-state reactive sintering. *Energies* **2018**, *11*, 3083. [\[CrossRef\]](#)
45. Wattanathana, W.; Veranitisagul, C.; Wannapaiboon, S.; Klysubun, W.; Koonsaeng, N.; Laobuthee, A. Samarium doped ceria (SDC) synthesized by a metal triethanolamine complex decomposition method: Characterization and an ionic conductivity study. *Ceram. Int.* **2017**, *43*, 9823–9830. [\[CrossRef\]](#)
46. Nantharak, W.; Wattanathana, W.; Klysubun, W.; Rimpongpisarn, T.; Veranitisagul, C.; Koonsaeng, N.; Laobuthee, A. Effect of local structure of Sm³⁺ in MgAl₂O₄:Sm³⁺ phosphors prepared by thermal decomposition of triethanolamine complexes on their luminescence property. *J. Alloys Compd.* **2017**, *701*, 1019–1026. [\[CrossRef\]](#)
47. Zhu, B.; Liu, X.; Zhu, Z.; Ljungberg, R. Solid oxide fuel cell (SOFC) using industrial grade mixed rare-earth oxide electrolytes. *Int. J. Hydrogen Energy* **2008**, *33*, 3385–3392. [\[CrossRef\]](#)

-
48. Bae, K.; Kim, D.H.; Choi, H.J.; Son, J.-W.; Shim, J.H. High-performance protonic ceramic fuel cells with 1 μm thick $\text{Y:Ba}(\text{Ce}, \text{Zr})\text{O}_3$ electrolytes. *Adv. Energy Mater.* **2018**, *8*, 1801315. [[CrossRef](#)]
 49. Bae, K.; Lee, S.; Jang, D.Y.; Kim, H.J.; Lee, H.; Shin, D.; Son, J.-W.; Shim, J.H. High-performance protonic ceramic fuel cells with thin-film yttrium-doped barium cerate–zirconate electrolytes on compositionally gradient anodes. *ACS Appl. Mater. Interfaces* **2016**, *8*, 9097–9103. [[CrossRef](#)]
 50. Liu, Y.; Guo, Y.; Ran, R.; Shao, Z. A novel approach for substantially improving the sinterability of $\text{BaZr}_{0.4}\text{Ce}_{0.4}\text{Y}_{0.2}\text{O}_{3-\delta}$ electrolyte for fuel cells by impregnating the green membrane with zinc nitrate as a sintering aid. *J. Membr. Sci.* **2013**, *437*, 189–195. [[CrossRef](#)]
 51. Nasani, N.; Ramasamy, D.; Mikhalev, S.; Kovalevsky, A.; Fagg, D.P. Fabrication and electrochemical performance of a stable, anode supported thin $\text{BaCe}_{0.4}\text{Zr}_{0.4}\text{Y}_{0.2}\text{O}_{3-\delta}$ electrolyte protonic ceramic fuel cell. *J. Power Sources* **2015**, *278*, 582–589. [[CrossRef](#)]